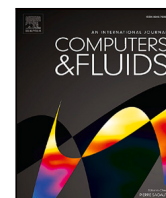# Investigation of low-dissipation low-dispersion schemes for incompressible and compressible flows in scale-resolving simulations

N.B. When citing this work, cite the original published paper.

(article starts on next page)

Investigation of low-dissipation low-dispersion schemes for incompressible and compressible flows in scale-resolving simulations

Magnus Carlsson [a,*], Lars Davidson [a], Shia-Hui Peng [a,b], Sebastian Arvidson [a,c]

[a] *Division of Fluid Dynamics and Maritime Sciences, Chalmers University of Technology, Gothenburg, SE-412 96, Sweden*
[b] *Swedish Defence Research Agency, FOI, Stockholm, SE-16490, Sweden*
[c] *Propulsion Systems, Saab Aeronautics, Linkoping, SE-581 88, Sweden*

ARTICLE INFO

ABSTRACT

A comprehensive study is conducted on a second-order low-dissipation low-dispersion (LD2) scheme in scale-resolving simulations of both incompressible and compressible flows, using a node-based unstructured CFD solver. The scheme deploys a higher order central reconstruction of the face values (up to fourth-order on structured meshes) and a matrix dissipation formulation to reduce the dispersive and dissipative numerical errors. The LD2 scheme is examined for compressible flow cases involving shock discontinuities, LD2-Compressible (LD2C), and is verified in a classical shock-tube problem. The scheme is then further verified in Large-Eddy Simulations (LES) of decaying isotropic turbulence (DIT) in comparison with available experimental data. It is shown that in scale-resolving simulations, the LD2C scheme is able to significantly improve the prediction as compared to a conventional second-order central scheme. The scheme is then further assessed and verified in hybrid Reynolds-Averaged Navier–Stokes (RANS)-LES computations for the subsonic and supersonic turbulent channel flow, where excellent agreement with reference DNS and correlations are observed. Moreover, a supersonic base flow is simulated using hybrid RANS-LES, where improved predictions are observed. The LD2C scheme exploits a shock sensor incorporating vorticity and is shown to improve the prediction of the resolved shear stress in the shear layer of compression.

1. Introduction

Hybrid RANS-LES modeling (HRLM) is a computational technique considered to be more accurate than RANS and computationally more affordable than LES for the aeronautical industry. The key feature of HRLM is the RANS-type behavior in the vicinity of a solid boundary combined with LES in regions far away from the wall. Commonly used HRLM methods stem from the Detached Eddy Simulation (DES) by Spalart et al. [1] and extended by boundary-layer shielding, e.g. Delayed DES, which is considered to be the most mature for industrial use. A wide variety of additional methods exist such as Improved DDES (IDDES) [2], HYB0 [3,4], PANS [5] and ZDES [6].

The turbulence-resolving capability in LES mode of DES and hybrid RANS-LES approaches depends strongly on the choice of the LES length scale. In flows involving free shear layers, the choice of LES length scale is crucial in order to mitigate the "grey-area" problem, which delays the development of LES-resolved turbulence in the initial LES region adjacent to the RANS-LES interface. As a result, the accuracy of scale-resolving simulation in the focusing LES region may become significantly degraded. In order to have effective transition between the RANS and the LES region in free shear layers, Grey-Area Mitigation (GAM) methods modifying the LES-length scale may be employed [6,7].

To accurately capture resolved turbulent fluctuations, proper resolution of LES requires a minimal dissipative and minimal dispersion numerical scheme. A low-dissipative finite-volume scheme suitable for unstructured compressible solvers was developed by Probst et al. [8], where the added numerical dissipation was effectively reduced and demonstrated for wall-bounded scale resolving flow. The numerical dissipation of the scheme is controlled by a Jameson matrix dissipation scheme [9], in order to reduce the level of added numerical dissipation suitable for scale-resolving simulations. To further improve the capabilities of the numerical scheme, a low-dissipation and low-dispersion (LD2) scheme was formulated by Löwe et al. [10], where a higher order extrapolation of the face values is used to control and reduce the numerical dispersion errors.

A thorough study similar to [8,10] was conducted in Carlsson et al. [11] using the LD2 scheme in the compressible flow solver M-Edge [12] (former CFD solver Edge), which is an unstructured

---

* Corresponding author.
E-mail address: magnus.carlsson@chalmers.se (M. Carlsson).

finite-volume Navier–Stokes solver used to investigate complex aeronautical flows. A number of previous examples of aeronautical relevant cases using HRLM simulated with the solver have been well demonstrated, e.g. the flow over rudimentary landing gear [13], transonic duct flow [14,15] and flow around a three-element airfoil in high-lift configuration [16]. In the previous work [11], the LD2 scheme was applied to low-speed (nearly incompressible) turbulent flows, showing good results in LES of the turbulent channel flow case for a moderate Reynolds number and the decaying isotropic turbulence (DIT) in comparison to DNS and experiments.

In this work, we seek to adapt the LD2 scheme for scale-resolving of compressible flows. In addition to a verification of the LD2 scheme in hybrid RANS-LES of subsonic turbulent channel flow and DIT, three compressible flow cases are also considered here. The Sod shock tube case, hybrid RANS-LES of the super sonic channel flow and the supersonic base flow (experimentally investigated by Herrin and Dutton [17]). These test cases are chosen to adapt and evaluate the numerical scheme in compressible scale-resolving simulations.

The shock capturing capabilities of the numerical scheme is important, and should not interfere with the scale-resolving properties. In the original formulation by Jameson, a sensor similar to the second derivative of the pressure was formulated to identify shock-waves [9]. A different variant of sensor targeting to minimize excessive dissipation in shock/turbulence interaction in LES was formulated by Ducros [18]. The sensor is a slight modification to Jameson's sensor and involves the local flow vorticity to identify regions with resolved turbulence.

The paper is organized as follows. The numerical method is outlined in Section 2 and the turbulence models used in the paper is presented in Section 3. Results and evaluation of the numerical test are then presented in Section 4. Finally, the work is summarized and concluded in Section 5.

2. Numerical methods

The CFD solver used in the computations is the M-Edge code, which is an edge- and node-based Navier–Stokes flow solver applicable for both structured and unstructured grids [12,19]. The finite volume discretization is obtained by applying the integral formulation of the governing equations to a control volume surrounding node i,

$$\Delta V_i \frac{dq_i}{dt} + \sum_{j=1}^{nb_i} F_{ij} S_{ij} + \sum_{j=1}^{nb_i} G_{ij} S_{ij} = 0 \qquad (1)$$

where ΔV_i is the volume surrounding node i, $q_i = (\rho, \rho u, \rho v, \rho w, \rho E)$ are the unknown conservative variables at the node, F_{ij} and G_{ij} are the cell face convective and viscous fluxes between nodes i and j, and S_{ij} is the cell face area connecting the dual control volumes of the nodes. The number of neighbors adjacent to node i is denoted by nb_i. Eq. (1) is integrated in time using a 2nd-order backward Euler scheme, together with a dual-time stepping methodology using an explicit low-storage multistage Runge–Kutta scheme accelerated further by full-approximation storage (FAS) multigrid [9]. The boundary conditions have a weak formulation in which a set of temporary flow variables are computed and used in the calculations of the boundary flux added to the residual. The residual then updates all unknown variables including the boundary values [20].

Since the dispersion and dissipation, due to the convective term, are of interest, a detailed description of the theory and implementation follows below. The convective fluxes are discretized according to the central skew-symmetric energy preserving formulation of Kok [21], together with a Jameson–Schmidt–Turkel (JST) artificial matrix dissipation [22,23]

$$F_{ij} = \tilde{F}_{ij}(q_L, q_R) - D_{ij}(q) \qquad (2)$$

where q_L, q_R are extrapolated face values according to a central scheme for reducing dispersion errors [10], and the subscripts L and R refer

to the left and right states at the cell face ij. The matrix dissipation D_{ij} is the JST artificial viscosity term included for increased numerical stability on hybrid grids, since the central skew-symmetric formulation by Kok does not provide any numerical dissipation to the scheme.

2.1. Numerical dispersion

The skew-symmetric energy preserving formulation by Kok [21] relies on a particular discretization of the convective terms in the mean flow equations such that good dispersion properties are obtained. The averaged cell face values in the convective numerical flux are formulated as

$$\tilde{F}_{ij} = \begin{bmatrix} (\overline{\rho u})_{ij} \\ (\overline{\rho u \bar{u}} + \bar{p} I)_{ij} \\ (\overline{\rho u \tilde{E}} + \widetilde{p u})_{ij} \end{bmatrix}$$

$$= \begin{bmatrix} \frac{1}{2}(\rho_L u_L + \rho_R u_R) \\ \frac{1}{2}(\rho_L u_L + \rho_R u_R)\frac{1}{2}(u_L + u_R) + \frac{1}{2}(p_L + p_R) I \\ \frac{1}{2}(\rho_L u_L + \rho_R u_R)\left[\frac{1}{2}(u_L u_R) + \frac{C_L C_R}{\gamma(\gamma-1)}\right] + \frac{1}{2}(u_L p_R + u_R p_L) \end{bmatrix} \qquad (3)$$

The reader is referred to [10,21] for the particular choice of averaging ($\bar{(\cdot)}$ and $\tilde{(\cdot)}$) in Eq. (3). For the conventional central flux the subscripts L, R are given by the respective nodal values. In the low-dispersion scheme by Löwe et al. [10], the left and right face values of the velocity and pressure are extrapolated from the left and right node values, respectively, by using the gradient of the variable in the nodes, i.e.

$$u_L = u_i + \alpha \nabla u_i \cdot \mathbf{d}_{ij}, \quad u_R = u_j - \alpha \nabla u_j \cdot \mathbf{d}_{ij}$$
$$p_L = p_i + \alpha \nabla p_i \cdot \mathbf{d}_{ij}, \quad p_R = p_j - \alpha \nabla p_j \cdot \mathbf{d}_{ij} \qquad (4)$$

where $\mathbf{d}_{ij}$ is the distance vector between the two nodes. In this work, the gradients are evaluated with a Green–Gauss' approximation. α is a parameter that can be chosen to reduce the dispersion error for a specific range of wave numbers. Note that the speed of sound and density is not extrapolated in the original scheme, since the effects of extrapolation of these quantities were argued to be small as reported by Löwe et al. [10]. However, Löwe's formulation was only evaluated for subsonic flow cases. For compressible flow cases involving shock waves, see Section 4, we evaluate further the extrapolation of density and speed of sound as well in the following form,

$$\rho_L = \rho_i + \alpha \nabla \rho_i \cdot \mathbf{d}_{ij}, \quad \rho_R = \rho_j - \alpha \nabla \rho_j \cdot \mathbf{d}_{ij}$$
$$c_L = c_i + \alpha \nabla c_i \cdot \mathbf{d}_{ij}, \quad c_R = c_j - \alpha \nabla c_j \cdot \mathbf{d}_{ij} \qquad (5)$$

A theoretical analysis of the dispersion properties of α for an analytical case is given in Section 2.3.

2.2. Numerical dissipation

2.2.1. Matrix dissipation

The artificial matrix dissipation [22] in Eq. (2) is given by

$$D_{ij}(q) = \left|\frac{\partial F}{\partial q}\right|_{ij} [\varepsilon_{ij}^{(2)}(q_i - q_j) + \varepsilon_i^{(4)} L(q_i) - \varepsilon_j^{(4)} L(q_j)] \qquad (6)$$

where L is the undivided Laplacian and the convective flux Jacobian $\left|\frac{\partial F}{\partial q}\right|_{ij} = R_{ij} |\Lambda|_{ij} R_{ij}^{-1}$ is computed and diagonalized according to Langer [24]. A Harten type entropy fix [25] is employed to prevent vanishing eigenvalues of $|\Lambda|_{ij}$, and are limited so that they are larger than 30% of the spectral radius. The second order dissipation scaling parameter $\varepsilon_{ij}^{(2)}$ in Eq. (6) is only active in the presence of strong discontinuities (i.e. for high speed flows with shocks) and can be omitted when low Mach number flow cases are considered. The parameters $\varepsilon_i^{(4)}$ and $\varepsilon_j^{(4)}$ are given by, respectively,

$$\varepsilon_i^{(4)} = \varepsilon^{(4)} \left(\frac{\lambda_i}{2\lambda_{0ij}}\right)^p, \quad \varepsilon_j^{(4)} = \varepsilon^{(4)} \left(\frac{\lambda_j}{2\lambda_{0ij}}\right)^p,$$

$$\lambda_i = \sum_{k=1}^{nb_i}(u_{ik} n_{ik} + c_{ik}) S_{ik}, \quad \lambda_{0ij} = (|u_{ij} n_{ij}| + c_{ij}) S_{ij} \qquad (7)$$

where $u_{ij} = (u_i + u_j)/2$ and $c_{ij} = (c_i + c_j)/2$ denote, respectively, the flow velocity and speed of sound at the control volume face. The normal direction of the control surface to the edge between nodes i and j is denoted by n_{ij}. The purpose of the additional scaling with the local convective eigenvalues (λ_i, λ_j and λ_{0ij}) in Eq. (7) is to apply extra dissipation for highly stretched cells in direction of the cell stretching, for example in near wall boundary layer flows or free shear layer flows resolved by an anisotropic grid. This is a desired effect to improve the robustness of the discretization [26]. The factor p is chosen to have a close resemblance with the Martinelli [27] eigenvalue scaling for structured grids ($p = 0.3$). Note that by setting $p = 0$ we have $\varepsilon_i^{(4)} = \varepsilon_j^{(4)} = \varepsilon^{(4)}$. The fourth-order scaling parameter

$$\varepsilon^{(4)} = \max[0, \kappa^{(4)} - \varepsilon_{ij}^{(2)}] \tag{8}$$

is deactivated in the vicinity of shocks. Here, $\kappa^{(4)}$ is a global scaling parameter, where a typical value of $\kappa^{(4)}$ used in RANS simulations varies often with a value set between $1/128 - 1/64$ [24]. These values gives extra numerical dissipation to dampen numerical errors and converge to a steady state simulation quickly. However, as shown by Probst et al. [8,28] and Carlsson et al. [11], these values are not suitable for scale-resolving simulations and will severely dissipate resolved turbulence. LES of decaying grid turbulence and turbulent channel flow indicate that $1/512$ to $1/1024$ is a suitable range for $\kappa^{(4)}$ to allow a good trade off between convergence and numerical accuracy in scale-resolving simulations. The dissipation properties of this parameter is theoretically analyzed in Section 2.3 and is further explored in hybrid RANS-LES simulations in Section 4.

2.2.2. Low Mach number preconditioning

To enhance the convergence properties and accuracy for low Mach number flows the convective flux Jacobian in Eq. (6) is modified,

$$\left| \frac{\partial F}{\partial q} \right|_{ij} \longrightarrow P_{ij}^{-1} \left| \frac{\partial P F}{\partial q} \right|_{ij} \tag{9}$$

where the preconditioning matrix P_{ij} is based on Turkel's formulation [29]. The matrix $\left| \frac{\partial P F}{\partial q} \right|_{ij}$ in Eq. (9) is approximated by $\left| \frac{\partial \tilde{F}}{\partial q} \right|_{ij}$ [24], where the local speed of sound c in $\left| \frac{\partial F}{\partial q} \right|_{ij}$ has been replaced with an artificial speed of sound

$$\tilde{c} = \frac{c}{2} \sqrt{(1+\beta)^2 M^2 + 4\beta(1-M^2)} \tag{10}$$

where M is the local Mach number on the cell face. Both the preconditioning matrix and the convective flux Jacobian are functions of the local speed of sound given in Eq. (10), where the rescaled speed of sound decreases the difference between the largest and the smallest eigenvalues of the convective flux Jacobian in Eq. (9) for low Mach number flows. The function of preconditioning is controlled by

$$\beta = \min[\max(M^2, K M_\infty^2), 1] \tag{11}$$

where $\beta = 1$ gives no preconditioning, M_∞ is the free-stream Mach number and K is a tuning coefficient. In Eq. (9) the preconditioning can be turned off by setting K to a very large value ($K \to \infty$) to ensure $\beta = 1$. Typical values of K previously used in M-Edge vary between 1 and 4 for RANS simulations [30].

2.2.3. Shock capturing methods

For high speed flows the flow solver needs to be able to identify discontinuities in the presence of shock waves. A standard pressure-based sensor by Jameson [31] is often deployed, reading

$$\varepsilon_{ij}^{(2)} = \min[\kappa^{(2)} \max(\Psi_i, \Psi_j), 0.5] \tag{12}$$

where the sensor

$$\Psi_i = \frac{\left| \sum_{k=1}^{nb_i} (p_i - p_k) \right|}{\sum_{k=1}^{nb_i} (p_i + p_k)} \tag{13}$$

identifies regions with large pressure differences, e.g. shock waves, and returning a value close to unity. The numerical scheme is then reduced to a first-order scheme through Eqs. (12), (8) and (6). This is necessary since according to the work by Godunov [32], any monotonicity preserving numerical scheme in the presence of shock waves can be at most first-order accurate. For regions with a smooth continuously varying flow field the sensor given by Eq. (13) tends to be switched off and the scheme follows the fourth-order dissipation in Eq. (6). The value 0.5 in Eq. (12) limits the scheme to behave as a first-order upwind scheme in shock regions. The sensitivity of the sensor is modified through $\kappa^{(2)}$, where the value is tuned in a shock-tube case (Section 4.1) in this work.

A different sensor targeted for minimizing excessive dissipation in shockturbulence interaction in LES was formulated by Ducros as [18]

$$\Phi_i = \frac{(\nabla \cdot \mathbf{u})^2}{(\nabla \cdot \mathbf{u})^2 + (\nabla \times \mathbf{u})^2 + \epsilon} \tag{14}$$

where the sensor includes the dilation and the magnitude of vorticity of the flow field. Here, ϵ is a small number (10^{-30}) in order to avoid singularities. This limiter reduces the added dissipation in regions with resolved turbulence where the vortex motion becomes intensive. However, Eq. (14) alone is not capable of separating large dilatations (shocks) from small dilatational disturbances. Also, in flow regions where vorticity is negligible even very small dilatations will activate the switch. This can add dissipation where it is not wanted and can also introduce spurious oscillations, which both can degrade the accuracy of the solution. In order to mitigate these problems, the sensor given by Eq. (14) was multiplied [18] by the standard Jameson's sensor given by Eq. (13)

$$\varepsilon_{ij}^{(2)} = \min[\kappa^{(2)} \max(\Psi_i \Phi_i, \Psi_j \Phi_j), 0.5] \tag{15}$$

which was shown to effectively distinguish between shocks and compressible turbulence [18].

2.3. Analysis of numerical scheme

The dispersion and dissipation relations for the convective scheme can be analyzed by performing a semi-discrete stability analysis of a one-dimensional convection equation as discussed by Hirsch [33]. The numerical error of the discretization due to the convective term can be cast into a purely dissipative term, ε_D, and a purely dispersive term, ε_Φ, as a function of the wave numbers that the grid can resolve, $\phi \in [0, \pi]$. Here, values $\varepsilon_D < 1$ correspond to physical waves being dissipated by the convective scheme, and deviations from $\varepsilon_\Phi = 1$ corresponds to physical waves being transported with a negative ($\varepsilon_\Phi < 1$) or positive ($\varepsilon_\Phi > 1$) group velocity. The contribution to the dissipative error for smooth flows is a function of the fourth-order dissipation scaling parameter $\kappa^{(4)}$ (Eq. (8)), and the contribution to the dispersive error is a function of α (Eq. (4)). The corresponding errors for a set of chosen values are presented in Fig. 1.

The added numerical dissipation can effectively be lowered by reducing the value of $\kappa^{(4)}$, as indicated in Fig. 1(a). If one assumes that the added dissipation to the simulation should be only due to the SGS scales, it is therefore desirable to use as low value as possible of $\kappa^{(4)}$ in order to avoid dissipation of the smaller scales that the grid can resolve. However, in practical application some amount of numerical dissipation is often needed ($\kappa^{(4)} > 0$) in order to reach convergence.

The dispersion error is presented in Fig. 1(b). Taylor expansion shows that one has to choose $\alpha = 1/3$ to achieve fourth-order approximation of the derivative, which is the theoretically highest order for any α. The value $\alpha = 0$ yields a pure second-order central approximation. In [10], Löwe et al. investigated the values of $\alpha = 0.36$ and $\alpha = 0.4$, which showed better performance than $\alpha = 1/3$ in resolving features on a coarse grid for an analytical case, while admitting higher dispersion errors on finer grids compared to $\alpha = 1/3$. They concluded that $\alpha = 0.36$ gave the most favorable cancellation properties [10] and used it in a set of studies [28,34,35] for scale-resolving simulations.
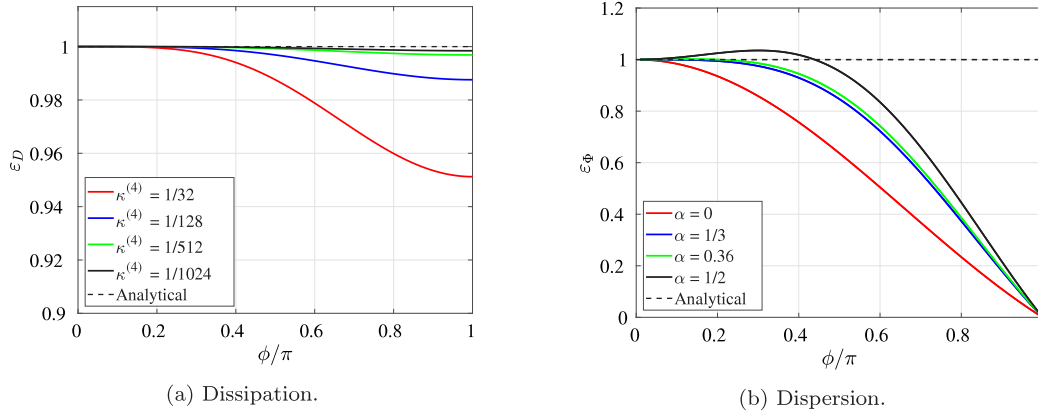
(a) Dissipation.   (b) Dispersion.

Fig. 1. Dissipation and dispersion relations.

However, the dispersion relation in Fig. 1 indicates that there is a small difference between $\alpha = 0.36$ optimized by Löwe et al. [10] and the value $\alpha = 1/3$ that gives the theoretically highest order. In Carlsson et al. [11], LES of fully developed channel flow and DIT using the LD2 scheme showed that in practical applications there is little difference between the values of $\alpha > 0$ shown in Fig. 1. Therefore, $\alpha = 1/3$ is chosen in the following analysis.

3. Turbulence modeling

For the hybrid RANS-LES computations of attached boundary layers with flow induced separation, we use the DDES approach [36]. The blending function between the RANS mode and the LES mode reads:

$$l_{DDES} = l_{RANS} - f_d \max(0, l_{RANS} - l_{LES}) \tag{16}$$

where the enhanced boundary layer shielding function f_d blends between l_{RANS} and l_{LES}, the RANS and LES length scales, respectively. The RANS-model then works as a hybrid RANS-LES model by replacing l_{RANS} by the hybrid length scale given by l_{DDES}. The LES length scale in (16) is given by

$$l_{LES} = C_{DES} \Psi \Delta \tag{17}$$

Here, C_{DES} is the modeling constant and is code dependent, and Ψ is a correction function to avoid (an unphysical) low Reynolds number damping in the LES region [36]. In the original formulation of the DDES model, the length scale in Eq. (17) is set to the maximum cell dimension Δ_{max}. In an edge-based code like M-Edge, it is defined as the maximum edge length of a dual control volume cell.

For scale-resolving simulation of wall bounded flows, the IDDES [2] is employed. The IDDES blends two branches, the DDES-like branch which should become active only when the inflow conditions do not have any turbulent content, and the WMLES-like branch intended to be active only when the inflow conditions used in the simulation are unsteady and impose some turbulent content and if the grid is fine enough to resolve boundary-layer dominant eddies. The blending function between the RANS mode and the LES mode reads:

$$l_{IDDES} = \tilde{f}_d(1 + f_e)l_{RANS} + (1 - \tilde{f}_d)l_{LES} \tag{18}$$

Here, $\tilde{f}_d$ is a function that blends between DDES and WMLES, and f_e is a function to enhance the RANS length scale in the vicinity of the RANS-LES interface in order to reduce the log-layer mismatch [2]. The LES length scale in Eq. (18) is given by Eq. (17) but the local filter-width Δ is replaced by

$$\Delta_{dw} = \min(\max[C_{dw}d_w, C_{dw}\Delta_{max}, \Delta_{wn}], \Delta) \tag{19}$$

The purpose of Δ_{dw} in Eq. (19) is to give a correct log-layer behavior in WMLES without the need to alter the value of the modeling constant

C_{DES} adapted to decaying grid turbulence. In Eq. (19), $C_w = 0.15$ and Δ_{wn} is the characteristic wall-normal cell size. For an unstructured edge-based solver as M-Edge, this quantity is not defined in a straightforward way. In this work, it is approximated by taking the difference between the maximum and the minimum cell face value of the wall distance d_w for a given cell. The cell face value is computed by the average of the two connecting nodes for a given edge. As underlying RANS models, the Spalart–Allmaras (SA) RANS model [37] and the Menter Shear-Stress Transport (SST) [38] are considered in this work. Note that the damping function in Eq. (17) is not needed for the SST model ($\Psi = 1$). The Δ_{max} length scale is used in Eqs. (17) and (19) unless otherwise stated.

3.1. Improved LES length scale

It has been shown in several studies that Δ_{max} often gives an excess SGS viscosity for flow cases involving free shear layers in LES mode (e.g. [7,39,40]). An alternative length scale to alleviate this problem was formulated by Shur et al. [7], where the length scale in Eq. (17) is replaced by $\tilde{\Delta}_\omega$ which is based on the local vorticity direction in the flow. For a hexahedral cell $\tilde{\Delta}_\omega$ is formulated as in Eq. (20)

$$\tilde{\Delta}_\omega = \frac{1}{\sqrt{3}} \max_{n,m} \|\mathbf{I}_n - \mathbf{I}_m\|, \quad \mathbf{I}_n = \mathbf{n}_\omega \times (\mathbf{r}_n - \mathbf{r}), \quad \mathbf{n}_\omega = \frac{\boldsymbol{\omega}}{\|\boldsymbol{\omega}\|} \tag{20}$$

where $\mathbf{n}_\omega$ is the unit vector aligned with the vorticity vector. This approach adapts the filter width to the local orientation of eddies, thus helping to reduce the well-known problem of delayed transition from RANS to LES modeling ("grey area") in the initial region of the shear layer. The factor $\frac{1}{\sqrt{3}}$ is needed to recover Δ_{max} for cubic cells in isotropic turbulence.

However, as pointed out in [7], replacing Δ_{max} with $\tilde{\Delta}_\omega$ is not enough to fully unlock the Kelvin–Helmholtz instability. To further force the reduction of the turbulent SGS viscosity in free shear layers the F_{KH} function is added to $\tilde{\Delta}_\omega$ to give

$$\Delta_{SLA} = \tilde{\Delta}_\omega F_{KH}(\langle VTM \rangle) \tag{21}$$

The F_{KH} function is based on a Vortex Tilting Measure (VTM) with the aim to detect Kelvin–Helmholtz like structures and rapidly reduce the LES filter width. Local VTM values are averaged over the current and closest neighboring cells, in order to make Δ_{SLA} behave as Δ_{max} in developed 3D turbulence. The averaged VTM quantity denoted $\langle VTM \rangle$ is close to zero in the quasi-2D regions of the flow, whereas in regions with fully developed turbulence it is of the order of 1.0. The Vortex Tilting Measure $\langle VTM \rangle$ in our implementation is computed as a volume average of the neighboring cells. The function F_{KH} takes values between zero and one, where one is its natural value and a reduction towards zero takes place in flows where Kelvin–Helmholtz like structures are detected. By achieving this additional reduction of

Table 1
Optimized parameters in numerical dissipation and dispersion for incompressible (LD2) and compressible (LD2C) flows.

Scheme	$\kappa^{(2)}$	Shock sensor	$\kappa^{(4)}$	$\alpha_u,\ \alpha_p$	$\alpha_\rho,\ \alpha_c$
Ref	5	Ψ_i	1/128	0	0
LD2 [28]	0	–	1/1024	1/3	0
LD2C	5	$\Psi_i \Phi_i$	1/512	1/3	1/3

the turbulent SGS viscosity, the two dimensional Kelvin–Helmholtz structures are able to break up and form three dimensional turbulent structures. For further information about F_{KH} and VTM, the reader is referred to Shur et al. [7].

4. Results and discussion

In this section, computations of several test cases are reported to investigate the effect of numerical dispersion (Section 2.1) and dissipation (Section 2.2) on resolved turbulence. In the present study we have examined a certain range of values of different parameters in test case computations. A summary of the optimal values for each parameter is shown in Table 1, which in the present study give the optimal performance, numerical stability and numerical accuracy in the computation of both incompressible and compressible flows. For reference, the LD2-related parameters adopted for incompressible flows by Probst et al. [28] and the values for the conventional second-order central scheme often used in RANS applications [24,26] are also shown in Table 1.

To establish the value of the shock capturing parameter $\kappa^{(2)}$ and the impact of the extrapolation parameter α in Eqs. (4) and (5) in the compressible flow adapted scheme, LD2-Compressible (LD2C), the Sod shock tube test case is evaluated in Section 4.1. The turbulence-resolving properties of the numerical scheme and calibration of the modeling constant C_{DES} are then investigated in simulation of DIT in Section 4.2.

The turbulence-resolving capabilities of the numerical scheme in wall-bounded flows in subsonic and supersonic conditions are investigated in Section 4.3 using IDDES. Having established the shock capturing and the turbulence resolving capabilities in supersonic flow, the LD2C scheme is further evaluated in hybrid RANS-LES of the supersonic base flow case in Section 4.4. In the supersonic base flow, the optimized numerical parameters using the test cases in Sections 4.1–4.3 are evaluated, together with the length scale Δ_{SLA} (Eq. (21)).

4.1. Sod Shock tube

The Sod Shock tube [41] is a Riemann problem commonly used to test the accuracy of computational methods for flow cases involving discontinuities. The problem consists of propagation of a shock wave, a contact discontinuity (surface that separates zones of different density and temperature), and an expansion fan. The Euler equations are solved to measure how well the numerical scheme can resolve the propagation speed of the rarefaction wave, the contact discontinuity and the shock discontinuity without introducing nonphysical oscillations. The test case is chosen to evaluate the effects of the second-order dissipation parameter $\kappa^{(2)}$ and the extrapolation (dispersion) parameter α. All simulations in this section exploit the standard Jameson sensor given by Eq. (13). In order to detect the contact discontinuity (since the pressure is continuous here), the sensor is modified to include the density as well, i.e.

$$\Psi_i = \max[\Psi_{i,p}, \Psi_{i,\rho}] \tag{22}$$

where $\Psi_{i,p}$ and $\Psi_{i,\rho}$ are the sensors of Eq. (13) evaluated with pressure and density, respectively.

The initial conditions are given by:

$$(p\ [\text{bar}], u\ [\text{m/s}], \rho\ [\text{kg/m}^3]) = \begin{cases} (1, 0, 1), & x \le 0.5 \\ (0.1, 0, 0.125), & x > 0.5 \end{cases} \tag{23}$$

The computational domain is given by $x \in [0, 1]$ m. Simulations are performed with constant time steps $\Delta t = 3.162 \cdot 10^{-6}$ s on a uniform grid composed of 200 grid points where $\Delta x = 0.005$ m, comparison between the exact solution and the numerical solution is made after 200 time steps (non-dimensional time $\tilde{t} = 0.2$).

Fig. 2 presents the density and temperature profiles. Figs. 2(a) and 2(b) shows the result for the conventional central scheme with no extrapolation ($\alpha = 0$, see Ref scheme in Table 1), and Figs. 2(c) and 2(d) for the LD2 scheme ($\alpha_p, \alpha_u = 1/3$, see Eq. (4) and Table 1). The peak oscillation at the normal shock location ($x \approx 0.85$ m) is reduced with the LD2 scheme using the higher order extrapolation for the pressure and velocity. However, the oscillation around the contact discontinuity ($x \approx 0.7$ m) remains. Nonetheless, approaching the normal shock, the oscillations are appreciably dampened by increasing the value of the second-order dissipation parameter $\kappa^{(2)}$ from 1 to 5.

With the LD2C scheme (see Table 1), an overall improvement is observed as seen in Figs. 2(e) and 2(f) by including the density and the speed of sound in the extrapolation scheme ($\alpha_\rho, \alpha_c = 1/3$, see Eq. (5)). This is particularly the case with $\kappa^{(2)} = 5$, by which the oscillations upstream of the normal shock have been effectively diminished and the peak near the contact discontinuity is also significantly mitigated. Therefore, the value $\kappa^{(2)} = 5$ is adopted for the LD2C scheme, which is used and further verified in the computations of the supersonic baseflow (see Section 4.4). It is noted here that the Ducros sensor (Eq. (15)) was verified as well for the LD2C scheme (not shown), and showed similar results as in Figs. 2(e) and 2(f).

4.2. Decaying isotropic turbulence

To assess the scale-resolving properties of the numerical scheme for nearly incompressible isotropic turbulence using the LES versions of the SA and SST turbulence models, the isotropic grid-generated turbulence experiment of Comte-Bellot and Corssin [42] is simulated as a temporal decay on an equidistant isotropic mesh. The incoming velocity field in the experiment was $U_0 = 10$ m/s, the grid spacing $M_g = 0.0508$ m, with a resulting Reynolds number $Re = \frac{U_0 M_g}{\nu} = 34\,000$. The kinetic energy and the turbulent spectra were reported for dimensionless times $\frac{tU_0}{M_g} \in \{42, 98, 171\}$. The reported spectra and wave number are made dimensionless to correspond to computational times of $\tilde{t} \in \{0, 0.87, 2.0\}$ [43].

The computational domain is a $2\pi \times 2\pi \times 2\pi$ cube discretized with N^3 equal sized Cartesian control volumes. Three grids have been considered with $N \in \{32, 64, 128\}$. The flow field is initialized with a prescribed velocity field of zero mean velocity. The initial fluctuating velocity distribution is obtained from the experimental energy distribution for $\tilde{t} = 0$ using an inverse Fourier transformation in a tool provided by Prof. Strelets at St. Petersburg Technical University. The other thermodynamic variables are initiated to uniform fields to simulate an initial turbulent Mach number of $M_t = 0.1$.

The chosen physical time step Δt corresponds to $CFL = 0.2$ based on the maximum initial velocity in the domain. A timestep of $\Delta t/2$ (namely $CFL = 0.1$) was tested for a couple of cases and gave no deviation in the result. Periodic boundary conditions are applied in all directions. The computed results are compared with the experiment by comparing the three dimensional spectra at times $\tilde{t} \in \{0.87, 2.0\}$. The results on three different grids for the LES models of SA and SST are shown in Fig. 3, where a sensitivity study on the different numerical settings given in Table 1 is made.

The modeling constant for the SA LES model is set to the standard value $C_{DES} = 0.65$ [36], the results are presented in Figs. 3(a), 3(c) and 3(e). For this test case the LD2 scheme is examined with two different
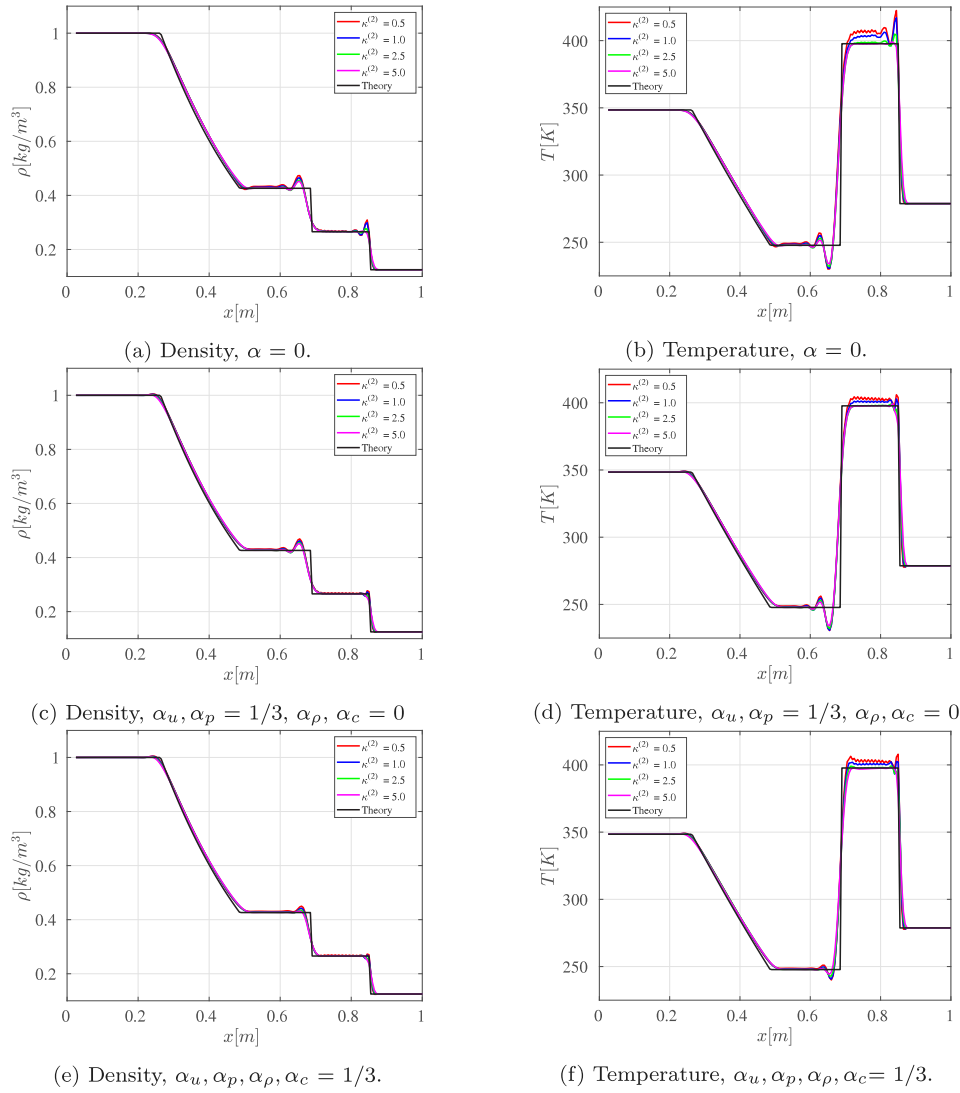
(a) Density, $\alpha = 0$.

(b) Temperature, $\alpha = 0$.

(c) Density, $\alpha_u, \alpha_p = 1/3, \alpha_\rho, \alpha_c = 0$

(d) Temperature, $\alpha_u, \alpha_p = 1/3, \alpha_\rho, \alpha_c = 0$

(e) Density, $\alpha_u, \alpha_p, \alpha_\rho, \alpha_c = 1/3$.

(f) Temperature, $\alpha_u, \alpha_p, \alpha_\rho, \alpha_c = 1/3$.

Fig. 2. Sod Shock tube [41] problem at $\tilde{t} = 0.2$ using different schemes.

values of $\kappa^{(4)}$, namely $1/512$ and $1/1024$. The results indicate that a relatively large value of $\kappa^{(4)}$ is only slightly more dissipative on the higher wave number for each grid. Nevertheless, the effect is very small and does not affect the overall performance of the scheme in this case. The results also show that the reference scheme (see Table 1) applies too much numerical dissipation, where the energy spectrum shows a too steep decay for the higher wave number on all three grids.

Results for the SST LES model is shown in Figs. 3(b), 3(d) and 3(f). Here, the model is run in its $k - \varepsilon$ mode using the standard value $C_{DES,k-\varepsilon} = 0.61$ [38]. Similar trends can be seen compared to the results of the SA model, the experimental spectra is well captured on all three grids for the LD2 scheme. The SST model was also run in its $k - \omega$ mode with $C_{DES,k-\omega} = 0.78$ (not shown), giving nearly identical results as in Figs. 3(b), 3(d) and 3(f).

The results shown in Fig. 3 indicate that the LD2 scheme with a value $\kappa^{(4)} = 1/512$ can accurately predict the correct decay of isotropic turbulence without the need to recalibrate the standard values of the modeling constant C_{DES} for the underlying turbulence models.

4.3. Fully developed channel flow

The fully-developed turbulent channel flow is a very useful test case for examining the capabilities of resolving turbulence in wall-bounded flows. The test case is employed for the implementation,

examination and validation of the numerical scheme for wall-bounded turbulence resolving simulations using IDDES (see Eq. (18)). In order to evaluate the methodology for aeronautical applications both subsonic and supersonic conditions and a wide Reynolds number range of the fully-developed turbulent channel flow are simulated.

The computational domain is a rectangular box of height 2δ (y), a length of $2\pi\delta$ (x), and a width of $\pi\delta$ (z), where δ is the half-channel height. Periodic boundary conditions are applied in the streamwise (x) and the spanwise (z) directions. To replicate the same wall boundary conditions as the reference DNS [44,45], no-slip adiabatic conditions are applied in the subsonic cases and no-slip isothermal conditions are applied in the supersonic cases.

To compensate for the lack of a pressure gradient $\partial p/\partial x$ driving the flow in the streamwise direction, the flow is driven by a forcing term, which enforces a specific massflow through the channel in order to achieve a target Reynolds number based on the bulk velocity Re_b. The target bulk Reynolds number is chosen to satisfy a corresponding Reynolds number based on the friction velocity Re_τ, where the target Re_τ is taken from DNS results or correlations. Subsonic or supersonic conditions are controlled by specifying the bulk Mach number M_b. The operating Re_b, Re_τ and M_b are defined as in Coleman et al. [46]

$$Re_b = \frac{\bar{\rho}_b \bar{u}_b \delta}{\bar{\mu}_w}, \quad M_b = \frac{\bar{u}_b}{\bar{c}_w}, \quad Re_\tau = \frac{\bar{\rho}_w u_\tau \delta}{\bar{\mu}_w} \tag{24}$$
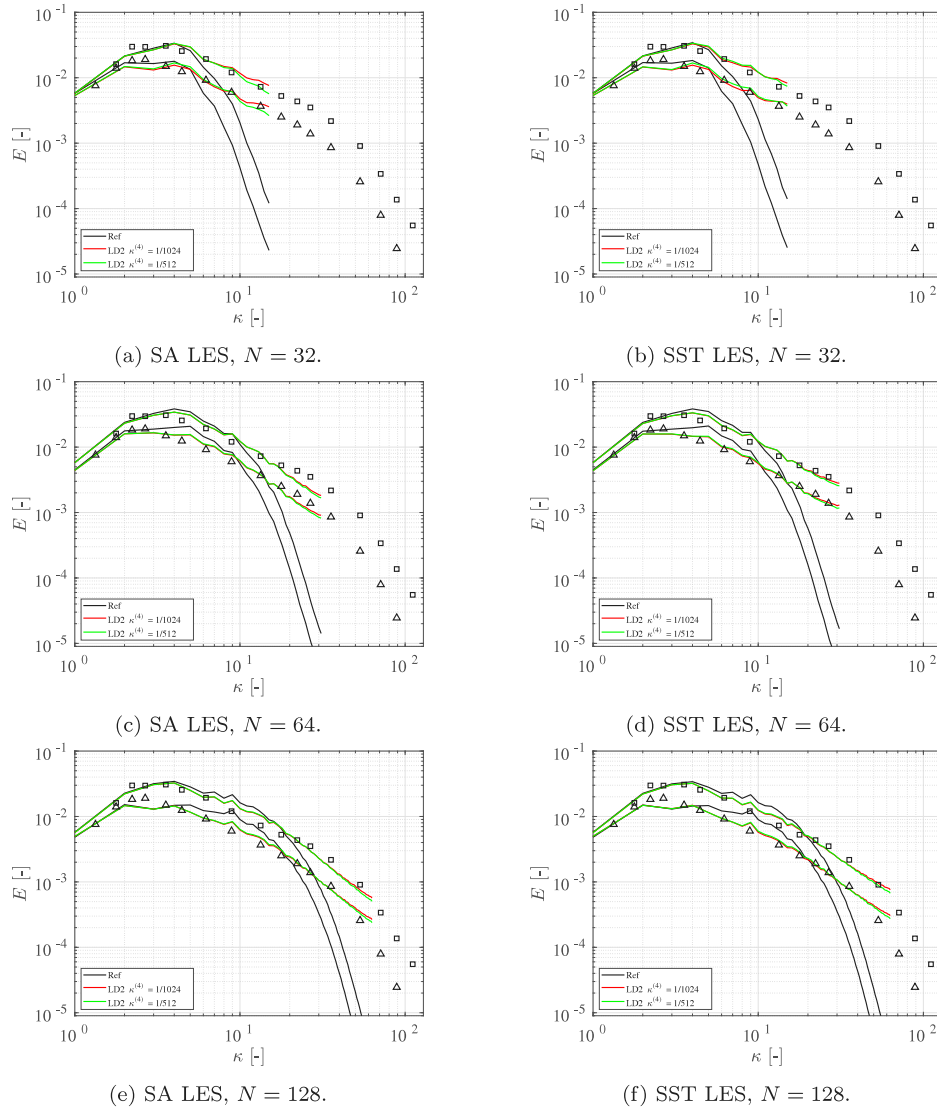
Fig. 3. DIT. Prediction of energy spectra in comparison with experimental data at non-dimensional times $\tilde{t} = 0.87$ (□) and $\tilde{t} = 2.0$ (△). Effects of numerical scheme. The legend is referred to Table 1.

Table 2
Summary of channel flow test cases and corresponding grid properties.

Case	Re_b	M_b	Re_τ	n_x	n_y	n_z	r	Δx^+	Δy^+	Δz^+
INC-395	6875	0.15	395	64	75	64	1.14	40	0.47–38	20
INC-2400	52 500	0.15	2400	64	102	64	1.14	239	0.45–219	120
INC-18000	483 000	0.15	18 000	64	132	64	1.14	1795	0.45–1697	898
CMP-500	7667	1.5	500	64	78	64	1.14	50	0.45–46	25
CMP-1015	17 000	1.5	1015	64	90	64	1.14	101	0.47–97	51
CMP-1015F	17 000	1.5	1015	128	118	128	1.11	50	0.5–40	25
CMP-5000	100 000	1.5	5000	64	112	64	1.14	518	0.5–515	259

where $\overline{\mu}_w$ is dynamic viscosity at the wall, $\overline{c}_w$ is the speed of sound at the wall and $u_\tau = \sqrt{\tau_w/\overline{\rho}_w}$ is the friction velocity. Details on the computational arrangement of the turbulent channel flow simulations are given in Table 2.

The different numerical settings (using low Mach number preconditioning, see Eq. (9)) in Table 1 are evaluated in the nearly incompressible regime ($M_b = 0.15$, cases INC-395, INC-2400 and INC-18000 in Table 2), where the meshing strategy follows WMLES practice according to Shur et al. [2]. The first off wall-normal node is placed at $y^+ \approx 0.5$ and a stretching factor $r = 1.14$ is used. A time step of $\Delta t^+ = 0.4$ is chosen in accordance to Probst et al. [28]. A random velocity field is generated by imposing synthetic fluctuations (STG by Shur et al. [47])

in a $y - z$ plane in the middle of the channel for one convective time units (CTU $= \delta/U_b$). The flow is then allowed to develop for two CTU and then averaged over ten CTU. Time averaged quantities are then averaged in the streamwise and spanwise directions.

Fig. 4 presents the mean velocity profile for the cases INC-395, INC-2400 and INC-18000 and the total stresses (modeled plus resolved stresses) for INC-395 using the SST version of IDDES. For comparison in this case, we have also included additional simulations with the LD2 scheme and the second-order dissipation activated by setting $\kappa^{(2)} = 5$, as in the LD2C scheme. This is to verify that the shock capturing scheme is automatically switched off for low speed incompressible flows. The results using the SA model are very similar (not shown). Excellent
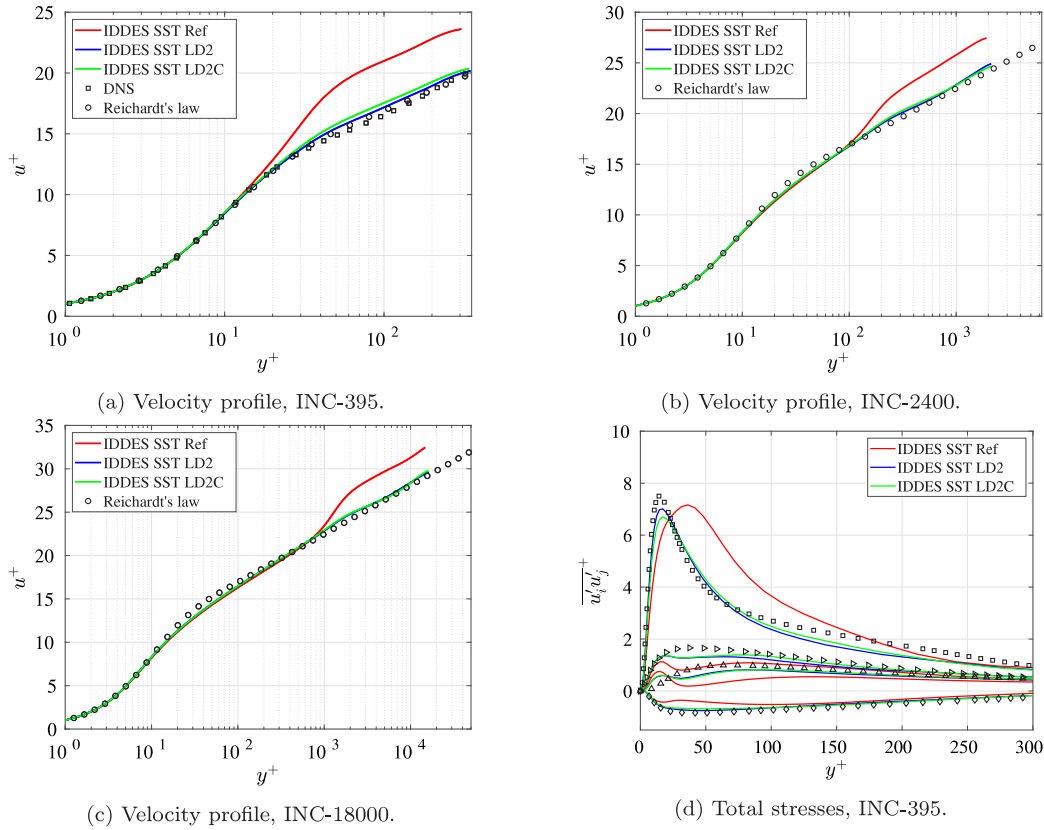
(a) Velocity profile, INC-395.

(b) Velocity profile, INC-2400.

(c) Velocity profile, INC-18000.

(d) Total stresses, INC-395.

Fig. 4. Fully developed turbulent channel flow with bulk Mach number $M_b = 0.15$ using SST-IDDES. Effects of numerical scheme. Results compared with Reichardt's law [48] and DNS [44]: $\square : \overline{u'u'}^+$, $\triangle : \overline{v'v'}^+$, $\triangleright : \overline{w'w'}^+$, $\diamond : \overline{u'v'}^+$.

agreement with reference DNS [44] for the velocity profile (Fig. 4(a)) and the total stresses (Fig. 4(d)) is achieved for the LD2 and LD2C schemes at $Re_\tau = 395$, where the peak of the streamwise stress $\overline{u'u'}^+$ is very well captured.

The velocity profile for the higher Reynolds number are in general well captured in comparison with the correlation by Reichardt [48], where a small log-layer mismatched can be observed at the RANS-LES interface (at around $y^+ \approx 200$ for $Re_\tau = 2400$ as shown in Fig. 4(b) and $y^+ \approx 2000$ for $Re_\tau = 18\,000$ as shown in Fig. 4(b)). On the other hand, the reference scheme (see Table 1) shows a significant log-layer mismatch for all Reynolds number. The velocity profile are well captured in the viscous sub-layer, buffer layer and the part of the log-layer where the IDDES operates in RANS mode, but fails as soon as the model switches to LES due to adding to much numerical dissipation. Overall, the results for the LD2 scheme are in line with previously reported results by Probst et al. [28].

In the supersonic channel flow simulations the bulk Mach number is set to $M_b = 1.5$. No low Mach number preconditioning is used. A time step $\Delta t^+ = 0.0015$ was chosen according to [49]. The same meshing strategy, initialization of flow field and averaging as in the incompressible cases are used. The Reynolds numbers for cases CMP-500 and CMP-1015 in Table 2 are chosen according to the DNS data available by Modesti et al. [45]. The Reynolds number for CMP-5000 was estimated using fully developed RANS to establish the relation between Re_b and Re_τ, since no reference DNS data was found by the author for this combination of higher Reynolds number and Mach number. However, by using proper velocity profile transformation the accuracy of the simulation can be estimated by using incompressible scaling laws.

As discussed by Coleman et al. [46], the so-called Van Driest transformation [50] can be employed for supersonic boundary layers in accounting for mean property variations in compressible turbulent wall-bounded flows. That means that, the density weighted velocity profile and Reynolds stresses

$$u_{vD}^+ = \int_0^{u^+} \sqrt{\frac{\overline{\rho}}{\rho_w}} \, \mathrm{d}\tilde{u}^+, \quad \overline{u_i'u_j'}^+_{vD} = \frac{\overline{\rho}}{\rho_w} \overline{u_i'u_j'}^+ \tag{25}$$

are expected to follow their incompressible counterparts. However, it has been shown in several studies, for example in [45,51,52], that the velocity transformation in Eq. (25) is inaccurate for non-adiabatic walls. Trettel and Larsson [52] proposed a different velocity transformation according to

$$u_T^+ = \int_0^{u^+} \sqrt{\frac{\overline{\mu}}{\mu_w}} \frac{\mathrm{d}y_T^+}{\mathrm{d}y^+} \, \mathrm{d}\tilde{u}^+, \quad y_T^+ = \frac{\overline{\rho}(\tau_w/\overline{\rho})^{1/2} y}{\overline{\mu}} \tag{26}$$
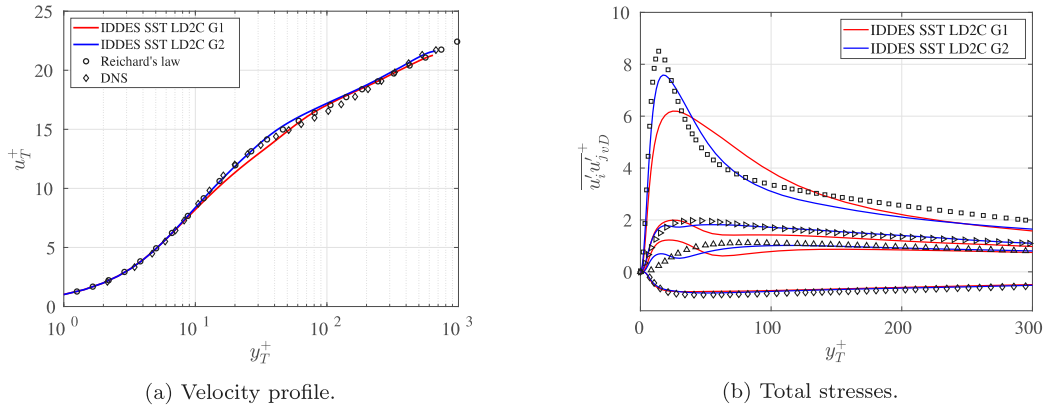
which was found to produce a good collapse of the mean velocity profile in comparison to standard incompressible scaling laws at different Reynolds numbers and Mach numbers of supersonic channel flows with iso-thermal walls. The velocity transformation in Eq. (26) is adopted in this work.

Fig. 5 presents the mean velocity profile for the cases CMP-500, CMP-1015 and CMP-5000 and the total stresses for CMP-5000 using SST-IDDES. Details about the grids used are given in Table 2. The results are similar to the subsonic case, the LD2 and LD2C schemes predicts the velocity profile very well in comparison to DNS data for cases CMP-500 and CMP-1015 (Figs. 5(a) and 5(b)), which collapses onto Reichardt's incompressible scaling law. Thus, the good agreement for the LD2 and LD2C schemes with the aforementioned law for the higher Reynolds number in CMP-5000 (Fig. 5(c)) is considered accurate. The reference scheme shows similar behavior as in the incompressible cases, the velocity profile is accurately predicted in the RANS part but is overestimated in the LES region.

However, the Reynolds stresses shown in Fig. 6(b) are not captured as well as in the incompressible case (Fig. 4(d)) for the LD2 and LD2C

(a) Velocity profile, CMP-500.

(b) Velocity profile, CMP-1015.

(c) Velocity profile, CMP-5000.

(d) Total stresses, CMP-1015.
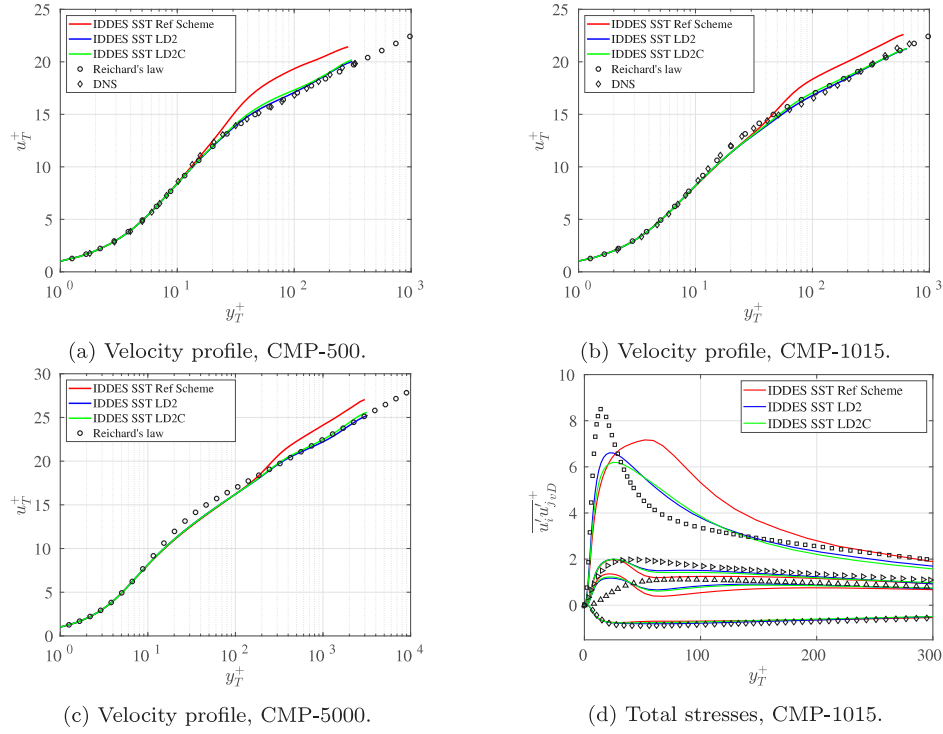
Fig. 5. Fully developed turbulent channel flow with bulk Mach number $M_b = 1.5$ at different Re_b using SST-IDDES. Effects of numerical scheme. Compared with Reichardt's law [48] and DNS data [45]: $\square$: $\overline{u'u'}_{vD}^{+}$, $\triangle$: $\overline{v'v'}_{vD}^{+}$, $\triangleright$: $\overline{w'w'}_{vD}^{+}$, $\diamond$: $\overline{u'v'}_{vD}^{+}$.

(a) Velocity profile.

(b) Total stresses.

Fig. 6. Fully developed supersonic channel flow with bulk Mach number $M_b = 1.5$ using SST-IDDES and LD2C. Effects of grid resolution, cases CMP-1015 (G1) and CMP-1015F (G2). Results compared with Reichardt's law [48] and DNS [45]: $\square$: $\overline{u'u'}_{vD}^{+}$, $\triangle$: $\overline{v'v'}_{vD}^{+}$, $\triangleright$: $\overline{w'w'}_{vD}^{+}$, $\diamond$: $\overline{u'v'}_{vD}^{+}$.

schemes using the same meshing strategy. For example, the peak value of the streamwise normal stress $\overline{u'u'}_{vD}^{+}$ is under predicted in comparison to the DNS result. In order to investigate the grid sensitivity, a finer grid is generated (see CMP-1015F in Table 2) with double grid resolution in the streamwise and spanwise directions, and a slightly finer resolution in the wall normal direction ($r = 1.11$).

The results for the LD2C scheme are shown in Fig. 6. The improved grid resolution yields a better match with the DNS velocity profile in the buffer layer (Fig. 6(a)) and the peak value of the streamwise stress is better predicted (Fig. 6(b)).

4.4. Supersonic base flow

A supersonic flow downstream of a blunt-based cylinder is characterized by expansion waves triggered due to the sharp turn of the flow over the base corner. A separation bubble with a low pressure recirculation region contained by a shear layer is formed behind the

base. The shear layer undergoes recompression and reattachment at the downstream end of the separation bubble along the symmetry axis. Due to the recompression, a shock wave is formed. An illustration of the flow field is shown in Fig. 7. This kind of flow is commonly found behind high speed projectiles, and the low pressure region behind the base causes drag which is a major part of the total drag. Thus, the modeling needs to be able to accurately predict the base pressure, along with other relevant properties such as the size of the recirculation bubble and turbulent properties subject to strong compressibility effects. For this flow, experimental data is available from the study by Herrin and Dutton [17].

The base flow has been employed in a number of modeling validations for compressible turbulent flows. The case was one of the test cases in the DESider EU Project [53]. Most of the contributors used SA-DES [54] with the standard length scale Δ_{max} and standard value of modeling constant $C_{DES} = 0.65$. Different grid resolution (0.9–3.6 Million cells) and grid type (structured and unstructured) were
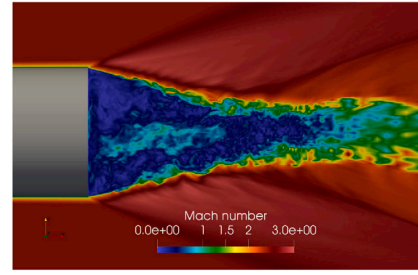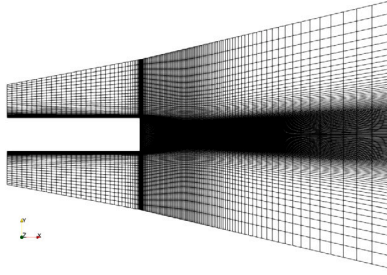
Fig. 7. Supersonic base flow. Illustration of computational domain (left) and visualization of flow field in the near wake of the cylinder (right). Simulation results acquired using LD2C on the finest grid.

investigated but a common trend was identified: good prediction of the base pressure with a flat profile as in the experiment, an over-estimated size of the recirculation bubble and underpredicted shear stress levels in the initial part of the separated shear layer. This was mainly attributed to the excessive levels of μ_t produced by Δ_{max} in the separated shear layer, which severely delayed the development of resolved turbulence. Simone et al. used the ZDES in two different studies [55,56], which employs the cubic root length scale $\Delta_{vol} = (\Delta_x \Delta_y \Delta_z)^{1/3}$ and a slightly lower value of the model constant ($C_{DES} = 0.55$). The studies included very fine grids (13.5 and 20.7 Million cells) and they reported very good agreement with experiment with regards to length of recirculation zone and the shear stress profiles. However, the backflow magnitude inside the bubble was greatly overpredicted yielding a wavy base pressure profile with the azimuth averaged pressure level significantly lower than that in the experiment. More recently, similar results was reported by Guseva et al. [57], where they employed the SA-DDES and the Δ_{SLA} length scale (Eq. (21)) on a relatively coarse mesh (2 Million cells) using $C_{DES} = 0.65$. They reported a considerable acceleration of the shear layer instability (due to the reduced levels of μ_t stemming from Δ_{SLA}) and a better general turbulence resolution in general, but did not capture a flat radial distribution of the base pressure. Nevertheless, the length scale was able to trigger resolved turbulence on a relatively coarse grid, which motivated the use of Δ_{SLA} to evaluate the impact of the numerical scheme in this study.

The Reynolds number based on the freestream velocity U_∞, base radius $R = 0.03175$ m and kinematic viscosity v is $Re_R = 1.632 \cdot 10^6$, with a freestream Mach number of $M_\infty = 2.46$. In the computation, we have used a computational domain (shown in Fig. 7) of size $L_x \times L_r = 23R \times 8R$ in the axial and radial direction, respectively. The length of the cylinder is set to $8R$, in order to match the upstream boundary layer momentum thickness with the experimental measurement at a distance of 1 mm up the base [53]. The downstream extension of the domain is $15R$ after the cylinder base. Characteristic Riemann conditions are imposed on all no-wall boundaries, and adiabatic wall conditions on the cylinder surfaces.

Three different grids are considered. A baseline grid with $N_{cells} = 1.82 \times 10^6$ cells (G1) is used, which was designed by FOI in the DESider project [53], see Figs. 8(a) and 8(b). Two new grids were generated, a grid with improved resolution in the shear layer consisting of $N_{cells} = 2.06 \times 10^6$ cells (G2), which was designed to match the resolution used in Guseva et al. [57]. An illustration of the grid is shown in Figs. 8(c) and 8(d). The third grid considered contains $N_{cells} = 8.51 \times 10^6$ cells (G3), where several cells in the axial and radial directions have also been added in the recirculation region downstream the base, see Figs. 8(e) and 8(f). A time step of $\Delta t = 1.0 \times 10^{-6}$ s (or equivalently $\Delta t = 0.018R/U_\infty$) is used, and the time sample for accumulation of turbulence statistics after a transient period of $90R/U_\infty$ is equal to $350R/U_\infty$. It is observed that for some of the simulations, the mean flow is still slightly asymmetric after time averaging, which is diminished by further averaging the solution over the azimuthal direction ϕ.

The hybrid RANS-LES method SA-DDES (Eq. (16)) using DES model constant $C_{DES} = 0.65$ is employed, as determined in the DIT case in

Section 4.2. The length scale Δ_{SLA} (Eq. (21)) is used as the filter width for the LES length scale in Eq. (17), where it was verified in DIT that the same spectra is acquired as for Δ_{max} (see Figs. 3(a), 3(c) and 3(e)) using the same value of the modeling constant.

Resolved instantaneous flow structures

In Fig. 9 the resolved turbulent structures are visualized using iso-surfaces of the Q-criterion at $Q(D/U_\infty)^2 = 10$. Similarly as reported by Guseva et al. [57], the Δ_{SLA} length scale reduces the eddy viscosity μ_t in the initial part of the shear layer to relatively small levels as in comparison to the upstream RANS modeled boundary layer. This allows unsteady turbulent motion to be triggered due to the strong shear. Thus, the creation of turbulent structures in the initial part of the shear layer using Δ_{SLA} is mainly governed by the amount of numerical dissipation introduced by the numerical scheme and the resolution of the grid.

The results of using the reference scheme for the three different grids are presented in Figs. 9(a) (G1), 9(c) (G2) and 9(e) (G3). There is a strong delay in the creation of the resolved structures in the vicinity of the trailing edge due to the high levels of numerical dissipation. Kelvin–Helmholtz (KH) like structures with large azimuthal coherence just downstream the base can be observed, where the two-dimensional structures break up into three-dimensional structures further downstream of the reattachment point. By refining the grid in the separated shear layer (G2), the delay is mitigated and hence the length of the recirculation bubble is reduced. The richness of the small scale turbulence is further increased by further refining the grid in the axial and azimuthal directions (G3), where an earlier breakup of the KH structures can be observed.

However, the effect of using the low dissipative LD2C scheme (Figs. 9(b), 9(d) and 9(f)) has a drastic effect on the flow field. A reduction in numerical dissipation from the shock capturing sensor (Ducros sensor in Eq. (14)) and the reduced overall dissipation unlocks the KH instability and substantially accelerates the transition to 3D turbulence in the separated shear layer. The overall richness of small scale turbulence on the coarse grid G1 is comparable to the fine grid G3 using the reference scheme.

Mean flow statistics

Time- and azimuth-averaged flow properties are shown in Fig. 10. The base pressure is presented in Fig. 10(a), where the experimental results yield a relatively flat profile around $C_p = -0.102$. The reference scheme is able to predict a flat profile on all three grids, but show a large variation of the mean value between G1 and the two other grids. The C_p values are in quite close agreement with the experiment on the axis for grids G2 and G3, but deviates more further away from the center. The simulations using the LD2C scheme show radial variations along the base and in general an under predicted base pressure coefficient. The difference between G1 and the other grids is smaller as compared to the reference scheme, but predicts too low pressure levels compared to the experimental data. However, a wavy base pressure profile and in general lower base pressure values are also observed in
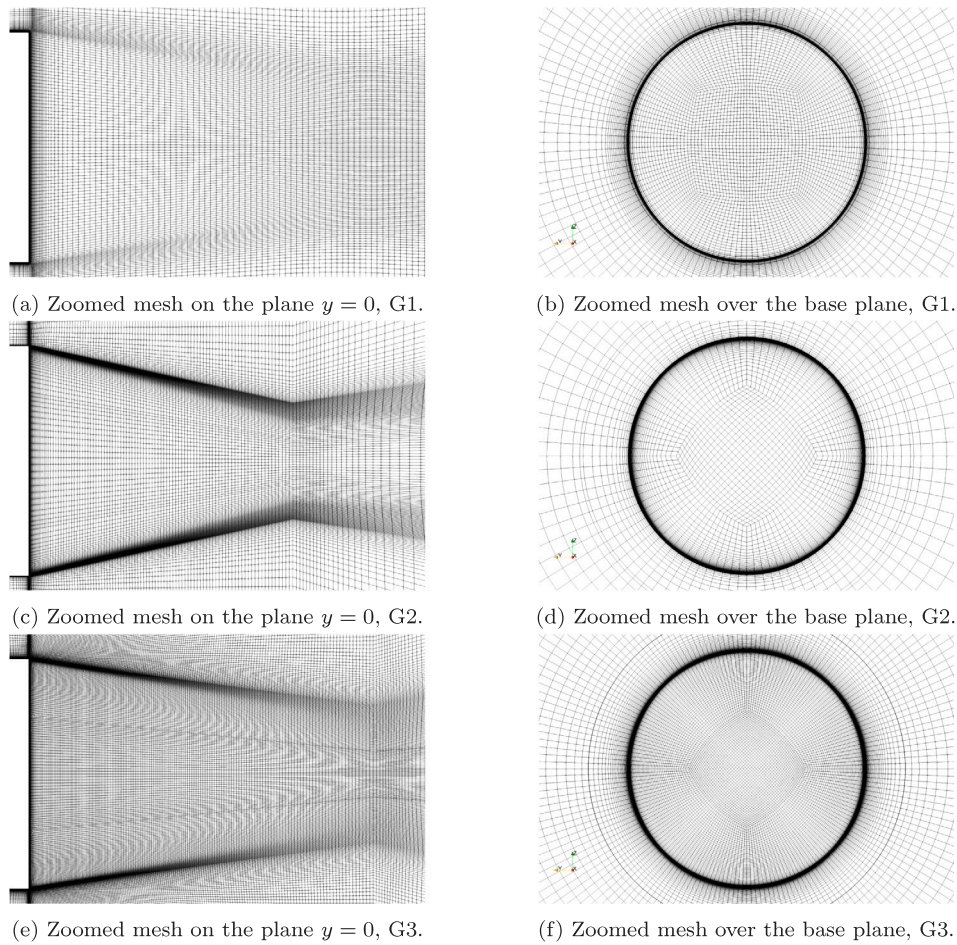
(a) Zoomed mesh on the plane $y = 0$, G1.

(b) Zoomed mesh over the base plane, G1.

(c) Zoomed mesh on the plane $y = 0$, G2.

(d) Zoomed mesh over the base plane, G2.

(e) Zoomed mesh on the plane $y = 0$, G3.

(f) Zoomed mesh over the base plane, G3.

Fig. 8. Supersonic base flow. Illustration of computational grids adopted to highlight grid sensitivity of resolving critical flow regions.

the works of Simone et al. [55] and Guseva et al. [57] as previously mentioned.

The previous trends can be explained by investigating the behavior of the centerline streamwise velocity component in Fig. 10(c). The reattachment point is poorly predicted using the reference scheme, which is $x/R \approx 4.0$ on G1 and $x/R \approx 3.0$ on G2 and G3, as compared to the experimental value $x/R = 2.67$. By using the LD2C scheme, the reattachment point ($x/R \approx 2.7$ on G2 and G3) and the flow downstream of $x/R > 2$ is much better predicted. On the other hand, the reverse flow is in general over predicted for the simulations using LD2C, which give rise to the under predicted base pressure levels in Fig. 10(a). The average Mach number and radial velocity at $x/R = 1.57$ are shown in Figs. 10(b) and 10(d). In general, the radial size of the recirculation bubble is under predicted for the simulations using LD2C scheme compared to the reference scheme, which indicates that the strength of the shear layer is under predicted.

Figs. 10(e) and 10(f) present a comparison of the predicted and measured fields of turbulent shear stresses at locations $x/R = 1.57$ and $x/R = 2.52$, respectively. The LD2C scheme is able to provide a much better agreement with the experimental data at $x/R = 1.57$, where the peak value of the shear stress is improved (which is further verifies the smaller resolved structures shown in Figs. 9(b), 9(d), 9(f)). A great over prediction of the shear stress at $x/R = 2.52$ can be observed for the simulations using the reference scheme, as is shown in Fig. 10(f). However, this effect is mitigated when using the LD2C scheme.

A general conclusion based on the simulations of the supersonic base flow is that improved numerics in the initial shear layer does not produce a better prediction of the base pressure profile, where a wavy pattern can be observed. However, the results are in line with

what is reported in Simone et al. [55] (where they use the AUSM + (P) numerical scheme and the ZDES model [55] on a much finer grid than G3) and in Guseva et al. [57] (where they use a blended fourth-order centered/third-order upwind biased convective scheme, the same length scale Δ_{SLA} and similar grid resolution as G2). A much better prediction of the resolved shear stress, both in the initial part of the shear layer and close to the attachment point, is achieved with the LD2C scheme.

5. Summary and conclusions

The low-dissipative low-dispersive scheme (LD2) by Löwe et al. [28] has been investigated in scale-resolving simulations. The original formulation considered only subsonic flow cases, but in this work the numerical scheme was investigated in and adapted to compressible flow cases, with the updated abbreviation LD2-Compressible (LD2C). The scheme reduces the dissipative and dispersive numerical errors connected to the convective term. The scheme controls added artificial dissipation through the matrix dissipation operator by Swanson and Turkel and can be adapted to low speed flows with a low Mach number preconditioner. The shock capturing parameter $\kappa^{(2)}$ and the global scaling parameter $\kappa^{(4)}$ are important parameters incorporated in the artificial dissipation formulation. The scheme exploits a shock sensor (formulated by Ducros [18]) targeting to minimize numerical dissipation in shock/turbulence interaction in scale-resolving simulations. Furthermore, the scheme employs a higher order central reconstruction to reduce the dispersive numerical error, controlled by an extrapolation parameter α.

The LD2C scheme was verified in scale-resolving simulations of two fundamental incompressible flows, the decaying isotropic turbulence
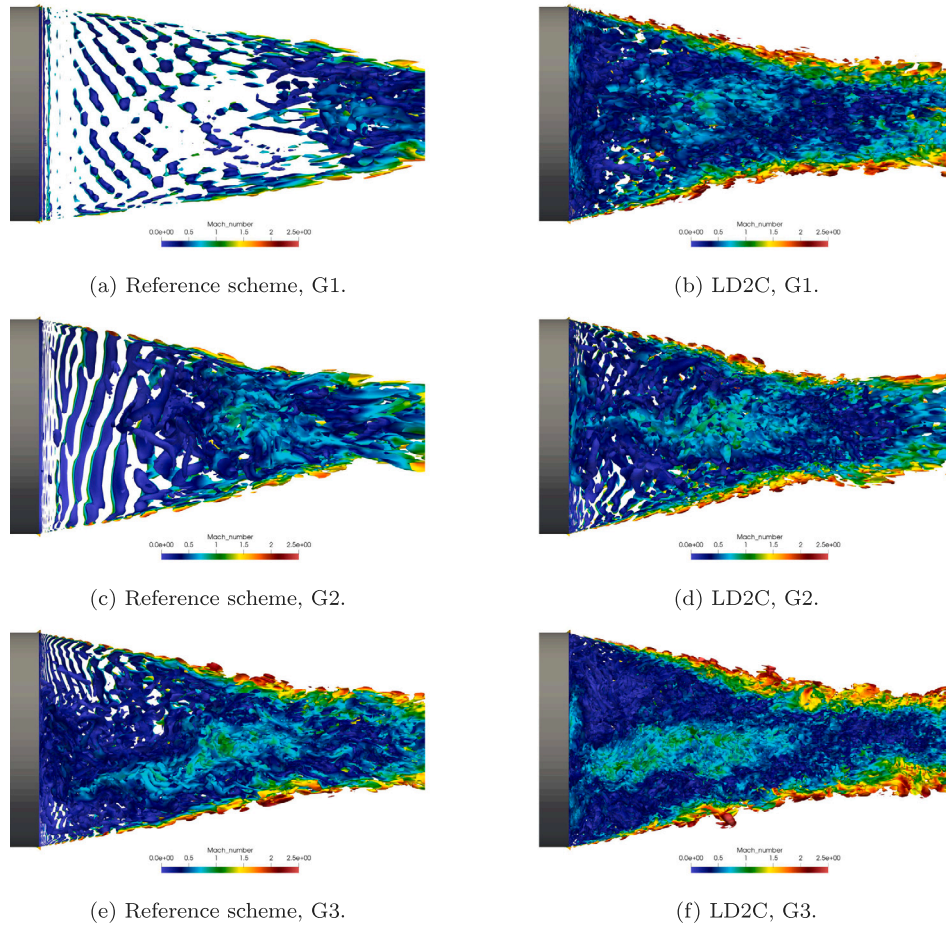
(a) Reference scheme, G1.

(b) LD2C, G1.

(c) Reference scheme, G2.

(d) LD2C, G2.

(e) Reference scheme, G3.

(f) LD2C, G3.

Fig. 9. Supersonic base flow. Resolved turbulent structures visualized using iso-surfaces of Q-criterion $Q(D/U_\infty)^2 = 10$. Colorbar indicates Mach number.

(DIT) and the subsonic turbulent channel flow. Furthermore, the LD2C scheme has been calibrated and evaluated in an inviscid fundamental test case involving a contact discontinuity and a normal shock wave. Further validation has been made in scale-resolving simulations of fully developed supersonic turbulent channel flow and supersonic base flow using hybrid RANS-LES modeling.

The first test case is the Sod shock tube. Validation against analytical solution showed that it is important to extrapolate both density and speed of sound to cell face using the extrapolation parameter α, in addition to only velocities and pressure as formulated in the LD2 scheme. This was needed to properly capture and mitigate oscillations in the vicinity of the normal shock wave and the contact discontinuity. The oscillation could effectively be reduced by setting the shock capturing parameter $\kappa^{(2)}$ to 5.

The second test case is decaying homogeneous isotropic turbulence with a turbulent Mach number of 0.1. It was shown that numerical dissipation associated to the convection term dominates the decay of turbulent kinetic energy, which becomes too strong at higher wave numbers. This could effectively be controlled by employing a low Mach number preconditioner and using a reduced value of $\kappa^{(4)}$ in the range of 1/512 or smaller. Results acquired on 32^3, 64^3, 128^3 grids give good agreement with reference experimental data using standard values of the modeling constant C_{DES} for the Spalart–Allmaras (SA) and Menter Shear Stress Transport (SST) as underlying turbulence models.

The third test case is the fully developed turbulent channel flow, investigated in subsonic and supersonic conditions at a wide range of Reynolds numbers. In validation against DNS data and correlation using SST-IDDES, the prediction of the mean velocity profile and the resolved turbulent stresses for $Re_\tau = \{395, 2400, 18\,000\}$ is excellent using the LD2C scheme, and is significantly improved as compared to a conventional second-order scheme. The results are consistent with previously reported results in [10] for the subsonic channel flow case. Moreover, the LD2C scheme shows good agreement with reference DNS using SST-IDDES in supersonic channel flow ($M_b = 1.5$) for $Re_\tau = \{500, 1015, 5000\}$, where the mean velocity profile and the Reynolds stresses are accurately predicted.

The final test case is the supersonic base flow. Hybrid RANS-LES simulations using SA-DDES showed a substantial improvement in the resolved turbulent structures triggered by the initial shear layer downstream the base, using the LD2C scheme and using the shear layer adapting LES length scale Δ_{SLA}. It is shown that the parameters optimized for the previous test cases remain suitable. The prediction agrees reasonably well with the measured data, but yield similar results to previously reported studies [55,57]. A shock-capturing scheme appropriately incorporating vorticity in the sensor formulation, e.g. by Ducros [18], was shown to improve capabilities in resolving the shear stress and contributing to grey-area mitigation in the initial part of the shear layer behind the base, compared to a standard scheme using the sensor formulation by Jameson [9].
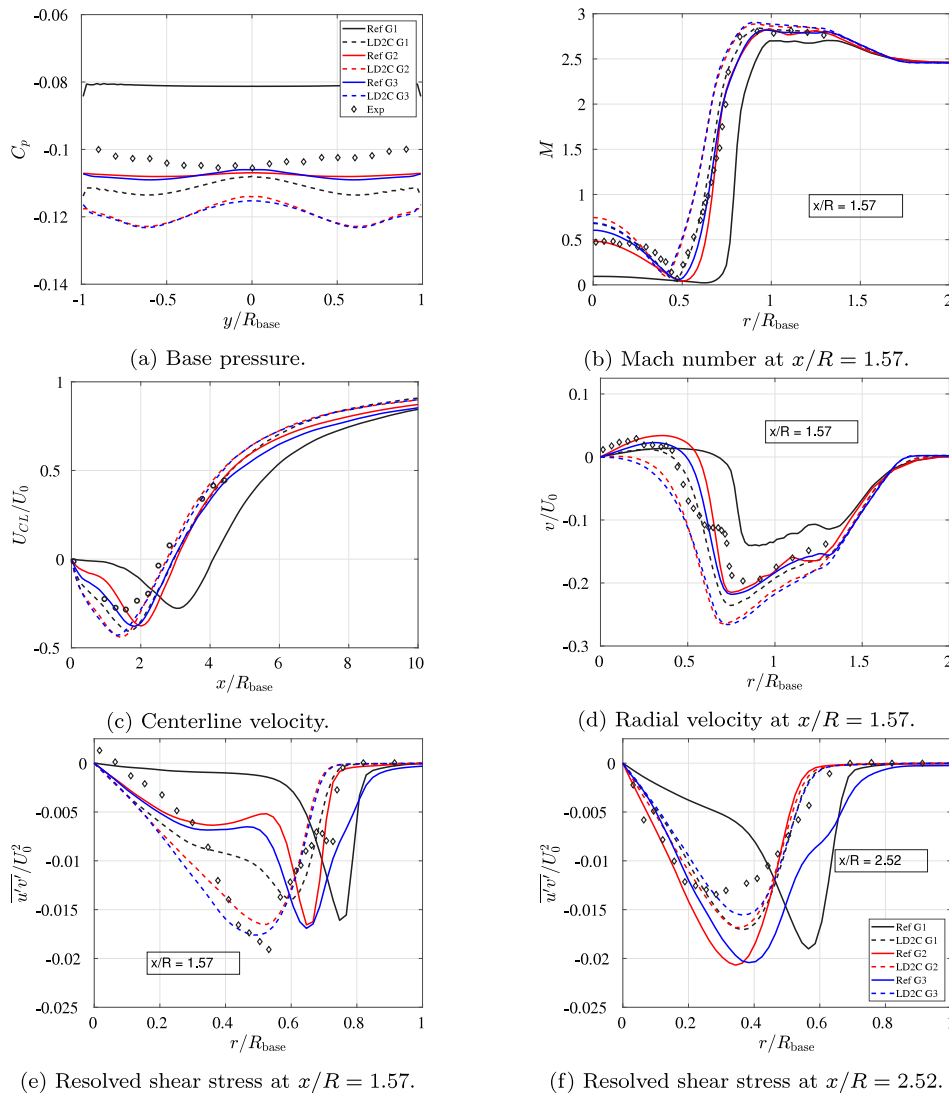
(a) Base pressure.

(b) Mach number at $x/R = 1.57$.

(c) Centerline velocity.

(d) Radial velocity at $x/R = 1.57$.

(e) Resolved shear stress at $x/R = 1.57$.

(f) Resolved shear stress at $x/R = 2.52$.

Fig. 10. Supersonic base flow. Effect of numerical scheme on SA-DDES prediction of the ϕ-averaged mean flow. Experiment by Herrin and Dutton [17] ($\diamond$).

CRediT authorship contribution statement

Magnus Carlsson: Conceptualization, Methodology, Investigation, Software, Writing – original draft, Validation, Visualization. **Lars Davidson:** Supervision, Resources, Writing – review & editing. **Shia-Hui Peng:** Conceptualization, Methodology, Supervision, Writing – review & editing. **Sebastian Arvidson:** Conceptualization, Project Administration, Funding acquisition, Supervision, Writing – review & editing.

Declaration of competing interest

The authors declare that they have no known competing financial interests or personal relationships that could have appeared to influence the work reported in this paper.

Data availability

Data will be made available on request.

References

[1] Spalart P, Jou W-H, Strelets M, Allmaras S. Comments on the feasibility of LES for wings, and on a hybrid RANS/LES approach. In: Advanced in DNS/LES. 1997.

[2] Shur ML, Spalart PR, Strelets MK, Travin AK. A hybrid RANS-LES approach with delayed-DES and wall-modelled LES capabilities. Int J Heat Fluid Flow 2008;29(6):1638–49. http://dx.doi.org/10.1016/j.ijheatfluidflow.2008.07.001.

[3] Peng SH. Hybrid RANS-LES modeling based on zero- and one-equation models for turbulent flow simulation. In: 4th international symposium on turbulence and shear flow phenomena, Vol. 3. 2005, p. 1159–64.

[4] Peng SH. Hybrid RANS-LES modelling with an energy backscatter function incorporated in the LES mode. 2012, p. 9. http://dx.doi.org/10.1615/ICHMT.2012.ProcSevIntSympTurbHeatTransfPal.260.

[5] Girimaji SS, Wallin S. Closure modeling in bridging regions of variable-resolution (VR) turbulence computations. J Turbul 2013;14(1):72–98. http://dx.doi.org/10.1080/14685248.2012.754893.

[6] Deck S. Recent improvements in the zonal detached eddy simulation (ZDES) formulation. Theor Comput Fluid Dyn 2011;26:1–28. http://dx.doi.org/10.1007/s00162-011-0240-z.

[7] Shur M, Spalart P, Strelets M, Travin A. An enhanced version of DES with rapid transition from RANS to LES in separated flows. Flow Turbul Combust 2015;95. http://dx.doi.org/10.1007/s10494-015-9618-0.

[8] Probst A, Reuß S. Scale-resolving simulations of wall-bounded flows with an unstructured compressible flow solver. In: Progress in hybrid RANS-LES modelling, Vol. 130. Springer; 2015, p. 481–91.

[9] Jameson A. Time-dependent calculations using multigrid with applications to unsteady flows past airfoils and wings. AIAA paper (91-1596), 1991.

[10] Löwe J, Probst A, Knopp T, Kessler R. Low-dissipation low-dispersion second-order scheme for unstructured finite-volume flow solvers. AIAA J 2016;54. http://dx.doi.org/10.2514/1.J054956.

[11] Carlsson M, Davidson L, Peng S, Arvidson S. Parametric investigation of low-dissipation low-dispersion schemes for unstructured flow solvers in large eddy simulation. In: 2020 AIAA scitech forum. 2020.

[12] Eliasson P. Edge, a Navier–Stokes solver for unstructured grids. In: Finite volumes for complex applications. CP849, vol. III, 2002, p. 527–34.

[13] Peng SH. Hybrid RANS-LES computations of turbulent flow over rudimentary landing gear. In: 31st AIAA applied aerodynamics conference. 2013, http://dx.doi.org/10.2514/6.2013-2913.

[14] Arvidson S, Peng S-H, Davidson L. Feasibility of hybrid RANS-LES modeling of shock/boundary-layer interaction in a duct. Not Numer Fluid Mech Multidiscip Des 2012;117:245–56. http://dx.doi.org/10.1007/978-3-642-31818-4_21.

[15] Arvidson S, Peng S-H, Davidson L. Prediction of transonic duct flow using a zonal hybrid RANS-LES modeling approach. Not Numer Fluid Mech Multidiscip Des 2015;130:229–41. http://dx.doi.org/10.1007/978-3-319-15141-0_18.

[16] Nebenführ B, Yao H, Peng SH, Davidson L. Hybrid RANS/LES simulations for aerodynamic and aeroacoustic analysis of a multi-element airfoil. In: 19th AIAA/CEAS aeroacoustics conference. 2013, http://dx.doi.org/10.2514/6.2013-2066.

[17] Herrin JL, Dutton JC. Supersonic base flow experiments in the near wake of a cylindrical afterbody. AIAA J 1994;32(1):77–83. http://dx.doi.org/10.2514/3.11953.

[18] Ducros F, Ferrand V, Franck N, Weber C, Darracq D, Gacherieu C, Poinsot T. LES of the shock/turbulence interaction. J Comput Phys 1999;152:517–49. http://dx.doi.org/10.1006/jcph.1999.6238.

[19] Eliasson P, Weinerfelt P. Recent applications of the flow solver edge. In: 7th Asian CFD conference. CP849, 2007.

[20] Eliasson P, Eriksson S, Nordström J. The influence of weak and strong solid wall boundary conditions on the convergence to steady-state of the Navier-Stokes equations. AIAA paper (2009-3551), 2009.

[21] Kok JC. A high-order low-dispersion symmetry-preserving finite volume method for compressible flow on curvilinear grids. J Comput Phys 2009;228:6811–32. http://dx.doi.org/10.1016/j.jcp.2009.06.015.

[22] Swanson RC, Turkel E. On the central-difference and upwind schemes. J Comput Phys 1992;101:292–306. http://dx.doi.org/10.1016/0021-9991(92)90007-L.

[23] Jameson A. Origins and further development of the Jameson–Schmidt–Turkel scheme. AIAA J 2017;55(5):1487–510. http://dx.doi.org/10.2514/1.J055493.

[24] Langer S. Investigations of a compressible second order finite volume code towards the incompressible limit. Comput & Fluids 2017;149:119–37.

[25] Harten A. J. Self adjusting grid methods for one-dimensional hyperbolic conservation laws. J Comput Phys 1983;50:235–69.

[26] Langer S. Agglomeration multigrid methods with implicit Runge–Kutta smoothers applied to aerodynamic simulations on unstructured grids. J Comput Phys 2014;277:72–100. http://dx.doi.org/10.1016/j.jcp.2014.07.050.

[27] Martinelli L. Calculation of viscous flows with multigrid methods (Ph.D. thesis), Princeton University; 1987.

[28] Probst S, Knopp T, Francois D, Grabe C, Landa T, Radespiel R. Scale-resolving simulations of the streamwise sortex downstream of a delta wing. AIAA J 2016;54. http://dx.doi.org/10.2514/1.J054957.

[29] Turkel E, Radespiel R, Kroll N. Assessment of preconditioning methods for multidimensional aerodynamics. Comput & Fluids 1997;26:613–43. http://dx.doi.org/10.1016/S0045-7930(97)00013-3.

[30] Peng S-H. On the implementation of local preconditioning methods in EURANUS. Tech. rep. FOI-R–0332–SE, Swedish Research Agency, FOI; 2001.

[31] Jameson A, Schmidt W, Turkel E. Numerical solution of the Euler equations by finite volume methods using runge kutta time stepping schemes. In: 14th fluid and plasma dynamics conference. 1981, http://dx.doi.org/10.2514/6.1981-1259.

[32] Godunov SK, Bohachevsky I. Finite difference method for numerical computation of discontinuous solutions of the equations of fluid dynamics. Mat Sbornik 1959;47(89):271–306.

[33] Hirsch C. Numerical computation of internal & external flows: fundamentals of numerical discretization. USA: John Wiley & Sons, Inc.; 1988.

[34] Probst A. Scale-resolving simulations on unstructured meshes with a low-dissipation low-dispersion scheme. In: New results in numerical and experimental fluid mechanics XI. Cham: Springer International Publishing; 2018, p. 489–98.

[35] Probst S, Knopp T, Francois D, Grabe C, Landa T, Radespiel R. Scale-resolving simulations of the streamwise vortex downstream of a delta wing. In: AIAA scitech 2019 forum. 2019, http://dx.doi.org/10.2514/6.2019-0331.

[36] Spalart P, Deck S, Shur M, Squires K, Strelets M, Travin A. A new version of detached-eddy simulation, resistant to ambiguous grid densities. Theor Comput Fluid Dyn 2006;20:181–95. http://dx.doi.org/10.1007/s00162-006-0015-0.

[37] Aupoix B, Spalart P. Extensions of the Spalart–Allmaras turbulence model to account for wall roughness. Int J Heat Fluid Flow 2003;24(4):454–62, Selected Papers from the Fifth International Conference on Engineering Turbulence Modelling and Measurements.

[38] Gritskevich M, Garbaruk A, Schütze J, Menter F. Development of DDES and IDDES formulations for the k-w shear stress transport model. Flow Turbul Combust 2012;88. http://dx.doi.org/10.1007/s10494-011-9378-4.

[39] Arvidson S, Davidson L, Peng S-H. Interface methods for grey-area mitigation in turbulence-resolving hybrid RANS-LES. Int J Heat Fluid Flow 2018;73:236–57. http://dx.doi.org/10.1016/j.ijheatfluidflow.2018.08.005.

[40] Arvidson S, Carlsson M, Nilsson S. Effect of LES length scale and numerical scheme in hybrid RANS-LES of free shear layer flows. In: International council of aeronauutical sciences (ICAS), Stockholm. 2022.

[41] Sod GA. A survey of several finite difference methods for systems of nonlinear hyperbolic conservation laws. J Comput Phys 1978;27(1):1–31. http://dx.doi.org/10.1016/0021-9991(78)90023-2.

[42] Comte-Bellot G, Corrsin S. Simple eulerian time correlation of full- and narrow-band velocity signals in grid-generated "isotropic" turbulence. J Fluid Mech 1971;48:273–337. http://dx.doi.org/10.1017/S0022112071001599.

[43] Yan J. CM, Thiele F. Investigation of alternative length scale substitutions in Detached-Eddy simulation. Flow Turbul Combust 2005;74:85–102. http://dx.doi.org/10.1007/s10494-005-6916-y.

[44] Moser R, Kim J, Mansour N. Direct numerical simulation of turbulent channel flow up to Re = 590. Phys Fluids 1999;11(4):943–5. http://dx.doi.org/10.1063/1.869966.

[45] Modesti D, Pirozzoli S. Reynolds and Mach number effects in compressible turbulent channel flow. Int J Heat Fluid Flow 2016;59:33–49. http://dx.doi.org/10.1016/j.ijheatfluidflow.2016.01.007.

[46] Coleman GN, Kim J, Moser RD. A numerical study of turbulent supersonic isothermal-wall channel flow. J Fluid Mech 1995;305:159–83. http://dx.doi.org/10.1017/S0022112095004587.

[47] Shur M, Spalart P, Strelets M, Travin A. Synthetic turbulence generators for RANS-LES interfaces in zonal simulations of aerodynamic and aeroacoustic problems. Flow Turbul Combust 2014;93:63–92. http://dx.doi.org/10.1007/s10494-014-9534-8.

[48] Reichardt H. Vollständige darstellung der turbulenten geschwindigkeitsverteilung in glatten leitungen. ZAMM J Appl Math Mech 1951;31(7):208–19. http://dx.doi.org/10.1002/zamm.19510310704.

[49] Gerolymos GA, Vallet I. Pressure, density, temperature and entropy fluctuations in compressible turbulent plane channel flow. J Fluid Mech 2014;757:701–46. http://dx.doi.org/10.1017/jfm.2014.431.

[50] Van Driest ER. Turbulent boundary layer in compressible fluids. J Aeronaut Sci 1951;18(3):145–60. http://dx.doi.org/10.2514/8.1895.

[51] Huang PG, Coleman GN, Bradshaw P. Compressible turbulent channel flows: DNS results and modelling. J Fluid Mech 1995;305:185–218. http://dx.doi.org/10.1017/S0022112095004599.

[52] Trettel A, Larsson J. Mean velocity scaling for compressible wall turbulence with heat transfer. Phys Fluids 2016;28(2):026102. http://dx.doi.org/10.1063/1.4942022.

[53] Haase W, Braza M, Revell A. DESider: A European effort on hybrid RANS-LES modelling. Notes on numerical fluid mechanics and multidisciplinary design, vol. 103, 2009, http://dx.doi.org/10.1007/978-3-540-92773-0.

[54] Spalart P. Strategies for turbulence modelling and simulations. Int J Heat Fluid Flow 2000;21(3):252–63. http://dx.doi.org/10.1016/S0142-727X(00)00007-2.

[55] Simon F, Deck S, Guillen P, Sagaut P. Reynolds-averaged Navier-Stokes/large-Eddy simulations of supersonic base flow. AIAA J 2006;44(11):2578–90. http://dx.doi.org/10.2514/1.21366.

[56] Simon F, Deck S, Guillen P, Sagaut P, Merlen A. Numerical simulation of the compressible mixing layer past an axisymmetric trailing edge. J Fluid Mech 2007;591:215–53. http://dx.doi.org/10.1017/S0022112007008129.

[57] Guseva E, Garbaruk A, Strelets M. Assessment of delayed DES and improved delayed DES combined with a shear-layer-adapted subgrid length-scale in separated flows. Flow Turbul Combust 2017;98. http://dx.doi.org/10.1007/s10494-016-9769-7.